barrier limit, the barrier to a reaction might more appropriately be in H rather than in G. This limit is reminiscent of collision theory[26]. High pressure may thus represent an opportunity for condensed-matter chemical kineticists to investigate systematically the behaviour of kinetic rate constants when kinetic barriers vanish under controllable conditions.

The increase of transport rate in the range 0–3 GPa is very large, implying a significant inverse effect on viscosity of certain rocks and magmas with depth. This is consistent with the experimental work of Kushiro on network structured melts. Our results may be highly relevant to subduction-zone magmatism in the mantle. In this setting partial melting produces magmas enriched in SiO_2. Although there is little experimental information on the competing effect of temperature on silica-rich melts at high pressure, we propose that such magmas may show a decrease in viscosity with depth until the migration barrier vanishes at 3 GPa (a depth of ~100 km), and then suddenly start to become more viscous. We expect that this increase in viscosity may impede silicic magma mobility deeper than 100 km. Interestingly, the predicted viscosity minimum coincides with the nearly constant depth to the Wadati–Benioff zone locating the subduction slab at ~100 km beneath most subduction-related volcanic fronts[27]. This constant depth seems to be largely unaffected by such factors as convergence rate or slab thermal structure. We speculate that the onset of an increasing magma viscosity at a 'universal' depth of 100 km, predicted from the present experimental results, may control this aspect of subduction-zone dynamics. There are many unanswered questions such as the effect of SiO_2 content and volatiles on the pressure of the viscosity minimum. The proposed magma viscosity minimum at 3 GPa is a testable hypothesis. Unfortunately, all existing high-pressure experimental data on magma viscosity are limited to 2.5 GPa. Viscosity measurements in the range 2.5 to 5 GPa should be considered a priority. □

Received 18 March; accepted 9 October 1997.

1. Kushiro, I. in *Physics of Magmatic Processes* (ed. Hargraves, R. B.) 93–120 (Princeton Univ. Press, Princeton, 1980).
2. Fratello, V. J., Hays, J. F. & Turnbull, D. Dependence of growth rate of quartz in fused silica on pressure and impurity content. *J. Appl. Phys.* **51,** 4718–4728 (1980).
3. Shimizu, N. & Kushiro, I. Diffusivity of oxygen in jadeite and diopsite melts at high pressure. *Geochim. Cosmochim. Acta* **48,** 1295–1303 (1984).
4. Goldmsith, J. R. Enhanced Al/Si diffusion in $KAlSi_3O_8$ at high pressures: the effect of hydrogen. *J. Geol.* **96,** 109–124 (1988).
5. Stebbins, J. F., McMillan, P. F. & Dingwell, D. B. (eds) *Structure, Dynamics and Properties of Silicate Melts* (Reviews in Mineralogy Vol. **32,** (Mineralogical Society of America, Washington, 1995).
6. Williams, Q. & Jeanloz, R. P. Spectroscopic evidence for pressure-induced coordination changes in silicate glasses and melts. *Science* **239,** 902–905 (1988).
7. Hemley, R. J., Jephcoat, A. P., Mao, H. K., Ming, L. C. & Manghnani, M. H. Pressure-induced amorphization of crystalline silica. *Nature* **334,** 52–54 (1988).
8. Tsuchida, Y. & Yagi, T. New pressure-induced transformations of silica at room temperature. *Nature* **347,** 267–269 (1990).
9. Meade, C., Hemley, R. J. & Mao, H. K. High pressure X-ray diffraction of SiO_2 glass. *Phys. Rev. Lett.* **69,** 1387–1390 (1992).
10. Nygren, E. *et al.* Pressure dependence of arsenic diffusivity in silicon. *Appl. Phys. Lett.* **47,** 105–107 (1985).
11. Lu, G.-Q., Nygren, E. & Aziz, M. J. Pressure-enhanced crystallization kinetics of amorphous Si and Ge: Implications for point defect mechanisms. *J. Appl. Phys.* **70,** 5323–5345 (1991).
12. Spaepen, F. & Turnbull, D. in *Laser Annealing of Semiconductors* (eds Poate, J. M. & Mayer, J. W.) 15–42 (Academic, New York, 1982).
13. Jackson, K. A., Uhlmann, D. R. & Hunt, J. D. On the nature of crystal growth from the melt. *J. Cryst. Growth* **1,** 1–36 (1967).
14. Walker, D., Carpenter, M. A. & Hitch, C. M. Some simplifications to multi-anvil devices for high pressure experiments. *Am. Mineral.* **75,** 1020–1028 (1990).
15. Hemley, R. J., Mao, H. K., Bell, P. M. & Mysen, B. O. Raman spectroscopy of SiO_2 glass at high pressure. *Phys. Rev. Lett.* **57,** 747–750 (1986).
16. Poe, B. T. *et al.* Silicon and oxygen self-diffusivities in silicate liquids measured to 15 gigapascals and 2800 Kelvin. *Science* **276,** 1245–1248 (1997).
17. Tse, J. S. & Klug, D. D. Mechanical instability of α-quartz: a molecular-dynamics study. *Phys. Rev. Lett.* **67,** 3559–3562 (1991).
18. Meade, C., Reffner, J. A. & Ito, E. Synchrotron infrared absorbance measurements of hydrogen in $MgSiO_3$ perovskite. *Science* **264,** 1558–1560 (1994).
19. Angell, C. A., Cheeseman, P. A. & Tamaddon, S. Pressure enhancement of ion mobilities in liquid silicates from computer simulation studies to 800 kilobars. *Science* **218,** 885–887 (1982).
20. Tsuneyuki, S. & Matsui, Y. Molecular dynamics study of pressure enhancement of ion mobilities in liquid silica. *Phys. Rev. Lett.* **74,** 3197–3200 (1995).
21. Spaepen, F. & Turnbull, D. Kinetics of motion of crystal–melt interfaces. *AIP Conf. Proc.* **50,** 73–83 (1979).
22. Fratello, V. J., Hays, J. F., Spaepen, F. & Turnbull, D. The mechanism of growth of quartz crystals into fused silica. *J. Appl. Phys.* **51,** 6160–6164 (1980).
23. Stolper, E. M. & Ahrens, T. J. On the nature of pressure-induced coordination changes in silicate melts and glasses. *Geophys. Res. Lett.* **14,** 1231–1233 (1987).
24. Stebbins, J. F., in *Structure, Dynamics and Properties of Silicate Melts* (eds Stebbins, J. F., McMillan, P. F. & Dingwell, D. B.) 191–246 (Mineralogical Society of America, Washington, 1995).
25. Vineyard, G. H. Frequency factors and isotope effects in solid state rate processes. *J. Phys. Chem. Solids* **3,** 121–127 (1957).
26. Laidler, K. J. *Chemical Kinetics* (Harper & Row, New York, 1987).
27. Gill, J. *Orogenic Andesites and Plate Tectonics* (Springer, Berlin, 1981).
28. Agee, C. B., Li, J., Shannon, M. C. & Circone, S. Pressure–temperature phase diagram for the Allende meteorite. *J. Geophys. Res.* **100,** 17725–17740 (1995).

Acknowledgements. This research was supported by the Harvard MRSEC. We thank R. P. Jeanloz for helpful discussions.

Correspondence should be addressed to M.J.A. (e-mail: maziz@harvard.edu).

Nonlinear ground-motion amplification by sediments during the 1994 Northridge earthquake

Edward H. Field*, Paul A. Johnson†‡, Igor A. Beresnev§ & Yuehua Zeng‖

* *Department of Earth Sciences, University of Southern California, Los Angeles, California 90089-0740, USA*
† *Los Alamos National Laboratory, Los Alamos, New Mexico 87545, USA*
‡ *Université Pierre et Marie Curie (Paris 6), Département d'Acoustique Physique, 4 Place Jussieu, 75252 Paris, France*
§ *Department of Earth Sciences, Carleton University, 1125 Colonel By Drive, Ottawa, Ontario K1S 5B6, Canada*
‖ *Seismological Laboratory, University of Nevada, Reno, Nevada 89557, USA*

It has been known since at least 1898 (ref. 1) that sediments can amplify earthquake ground motion relative to bedrock. For the weak ground motion accompanying small earthquakes, the amplification due to sediments is well understood in terms of linear elasticity (Hooke's law)[2], but there has been a long-standing debate regarding the amplification associated with the strong ground motion produced by large earthquakes. The view of geotechnical engineers, based largely on laboratory studies, is that Hooke's law breaks down at larger strains causing a reduced (nonlinear) amplification. Seismologists, on the other hand, have tended to remain sceptical of this nonlinear effect, mainly because the relatively few strong-motion observations seemed to be consistent with linear elasticity. Although some recent earthquake studies have demonstrated nonlinear behaviour under certain circumstances[3,4], the significance of nonlinearity for the type of stiff-soil sites found in the greater Los Angeles region remains unresolved[5]. Here we report that ground-motion amplification due to sediments for the main shock of the 1994 Northridge earthquake was up to a factor of two less than the amplification observed for its aftershocks. These observations imply significant nonlinearity in such amplification, and bring into question the use of measurements of weak ground motion to predict the strong ground motion at sedimentary sites.

We compiled data for all locations where both main-shock and aftershock recordings were obtained for the 1994 earthquake. The 21 resultant sites are listed in Table 1 and plotted in Fig. 1. On the basis of surface geology, 15 of these sites are categorized as alluvium (Quaternary sediments), two as soft rock (Tertiary units) and four as relatively hard rock (Mesozoic basement). Also shown in Fig. 1 are the epicentral locations of the 184 aftershocks used in this study, as well as the surface projection of the main-shock rupture distribution. To limit ourselves to a manageable quantity of data, we have used only aftershocks with a magnitude between 3.0 and 5.6.

To estimate site effects in the weak-motion aftershock recordings,

the shear-wave Fourier amplitude spectrum observed at the ith site for the jth event, $O_{ij}(f)$, is represented as

$$O_{ij}(f) = E_j(f)\,P_{ij}(f)\,S_i(f) \quad (1)$$

where f is frequency, $E_j(f)$ is the source effect of the jth event, $P_{ij}(f)$ is the path effect for the ith station and jth event, and $S_i(f)$ is the site response for the ith site. The path effect is specified as

$$P_{ij}(f) = r^{-1}\,e^{-\pi f T_s/Q(f)} \quad (2)$$

where r is the hypocentral distance measured from the aftershock location, T_s is the observed shear-wave travel time, and $Q(f)$ is the quality factor representing attenuation.

The essence of the site-response estimation is as follows. After correcting the observations for the path effect by assuming some $Q(f)$, we estimate the source effects from a site or average of sites, preferably on bedrock, assumed to have no significant site response. The response at the other sites is then estimated as the ratio between the path-corrected observations and the estimated source effects. In practice, however, the entire data set is usually solved simultaneously by some kind of generalized inversion of equation (1)[6], which provides a convenient mode of book-keeping when not all events are recorded at all sites. Of the many schemes that have been proposed, we follow that of Field and Jacob[7] to ensure reliable uncertainty estimates.

The main-shock response is estimated as for the aftershocks using equations (1) and (2). However, care must be taken in defining the hypocentral distance, r, because the spatial distribution of rupture (18 by 24 km; ref. 8) can be a significant fraction of the distance to each site. Care should also be taken in defining T_s because the rupture persists for several seconds. Therefore, some kind of average values of r and T_s must be used so that the effects of energy arriving from distances nearer and farther than r, as well as before and after T_s, are averaged out.

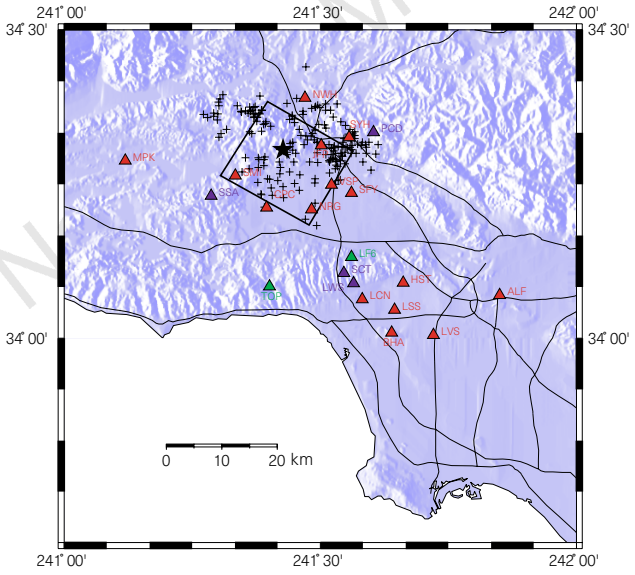

Figure 1 Relief map of the study region. The alluvium recording sites are shown as red triangles, the soft-rock sites as green triangles, and the hard-rock sites as blue triangles. Aftershock epicentres are shown with black crosses, and the main-shock rupture distribution[8] is outlined by the box. The fault plane dips 40° to the southwest, with the top edge at a depth of 5 km and the bottom edge at a depth of 20.4 km. The location of maximum slip is marked with the black star. All of the main-shock records were obtained from the strong-motion data archive of the Southern California Earthquake Center (SCEC)[17]. The aftershock data were obtained from either the United States Geological Survey (USGS)[18] or the SCEC data centre[19].

The estimates of both weak- and strong-motion site response obtained from equations (1) and (2) will be biased by any systematic difference between the actual path effects and those assumed in equation (2), or by any significant site response at the reference site(s). However, because our intention here is to identify any significant differences between the weak- and strong-motion response, and because the travel paths are similar for the main shock and aftershocks, these sources of bias will not influence the comparison as long as the same $Q(f)$ and reference-site definition are applied in both cases.

One additional complication is finite-source effects, such as directivity[9,10], in the strong-motion observations. These result from the large spatial extent of the main-shock rupture, where energy arriving from different locations on the fault plane may interfere constructively or destructively causing $E_j(f)$ to vary with site location. Therefore, appropriate spatial averages must be taken, or corrections applied, to avoid such biases.

Figure 2 shows the weak- and strong-motion site-response estimates averaged over the 15 quaternary alluvium sites. These estimates were computed relative to the average of the four hard-rock sites, and we followed Hartzell[11] in assuming $Q(f) = 150\,f^{1/2}$. The weak-motion response implies an amplification factor of ~3.1 at 1 Hz, decreasing to factors of ~2.5 and ~1.4 at 3 and 10 Hz, respectively. The strong-motion amplification factors are systematically less, being ~1.9 at 1 Hz, ~1.3 at 3 Hz, and ~0.8 (deamplification) at 10 Hz. This lower amplification for the main shock implies nonlinearity.

To test the null hypothesis that sediment amplification was similar for the main shock and the aftershocks, Fig. 3 shows the ratios of the weak- to strong-motion estimates at each sediment site. Also shown are the mean and 95% confidence region assuming a log-normal distribution[7]. The difference from unity is significant over almost the entire frequency band, and between 0.8 and 5.5 Hz at the 99% confidence level, leading to the rejection of the null hypothesis. In other words, sediment amplification seems to have been significantly less during the main shock, implying nonlinearity.

The difference as plotted in Fig. 3 is greatest between 2 and 4 Hz. For reference, the values of the individual ratios at 3 Hz are listed for each site in Table 1. One might ask whether the difference depends

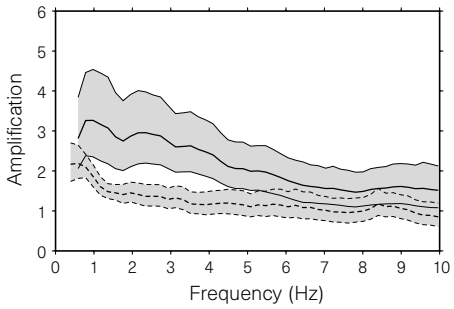

Figure 2 The mean and ±2 standard-deviation-of-the-mean confidence limits of the estimates of amplification at the 15 alluvium sites. The solid lines represent the weak-motion results for the aftershocks, and the dashed lines represent the strong-motion results for the main shock. The lower-frequency cutoffs reflect the lowest resolvable frequencies given seismometer and noise limitations. The Fourier amplitude spectra were computed from 20-s windows starting 1 s before the S-wave arrival, and were smoothed with a boxcar function that increased in width from 0.5 to 1.3 Hz between 0.5 and 10 Hz. The results presented here, however, do not depend on this particular spectral estimation technique. A stringent data elimination scheme was used to minimize the effects of noise[7], and the two horizontal components were geometrically averaged. Furthermore, to minimize the effects of location uncertainties, weak-motion recordings of aftershocks closer than 10 km were eliminated.

on the two highest ratios in Fig. 3 (VSP and JFP). In fact, at 3 Hz the highest 10 ratios (out of 15) must be removed from the average before the difference becomes insignificant at the 95% confidence level.

Many tests have been conducted to evaluate the robustness of this observation (E.H.F., Y.Z., P.A.J. and I.A.B., manuscript in preparation). As mentioned previously, any shortcomings of equation (2) in representing the path effects will be mapped onto the weak- and strong-motion estimates similarly, and therefore should not influence the ratios in Fig. 3. Nevertheless, we applied the Q models of Peng[12] and of Bonillia *et al.*[13], as well as a constant Q of 328, and found the results unchanged. Although bedrock sites can show their own unique behaviour[14,15], any significant site effect in our reference-site definition should influence both the weak- and strong-motion estimates similarly. Indeed, although the amplification levels shown in Fig. 2 depend on the reference definition, the significant difference shown in Fig. 3 does not depend on the inclusion of any particular rock site.

By far the most problematic source of bias could result from the large spatial extent of rupture during the main shock. For the strong-motion estimates r and T_s were determined from the location and timing of maximum slip as determined by the inversion of Wald *et al.*[8]. This point, shown as a star in Fig. 1, ruptured about 4.5 seconds after slip initiation at the hypocentre. However, we also computed r from all four corners of the rupture plane, and T_s from both the rupture initiation and termination 7 seconds later, and found the conclusions regarding the null hypothesis unchanged.

As an additional test of whether finite-source effects for the closest sites might be biasing the result, we re-did the analysis using only the more distant sites in the Los Angeles basin (LCN, HST, LSS, BHA, LVS and ALF) relative to the rock site SCT. Although not as pronounced, the difference still persists. For example, at 3 Hz the difference is a factor of 1.6 and is significant at the 95% confidence level. That the difference is lower is consistent with the notion that nonlinearity at the more distant sites, where ground motion levels are lower, will be less.

As a final test of whether finite-source effects might be masquerading as nonlinearity, we computed synthetic seismograms using the methodology and Northridge rupture model of Zeng and Anderson[16]. Specifically, for the 21 sites considered here, and using the one-dimensional velocity model given in their Table 2, we computed synthetic seismograms for the main shock and nine relatively small events distributed equally over the main-shock rupture plane. By conducting an analysis identical to that used to generate Figs 2 and 3, we have found no evidence for a significant bias due to finite source effects.

To infer the presence of nonlinear response amongst the myriad of competing effects, we have been forced to combine the results from numerous alluvium sites. However, by such averaging we sacrifice physical insight into the nature of the nonlinearity. Having convinced ourselves that the nonlinearity exists, we can now examine individual sites more carefully to detect shifts in resonant frequencies and/or reductions in amplification factors as a function of input amplitudes, both of which are symptomatic of nonlinear response. A sediment resonance that is clear in the weak-motion site-response estimate (for four of the sites, SMI, NWH, JFP and LF6) is conspicuous by its absence in the strong-motion results (again implying nonlinearity). Such observations will help test the validity of the laboratory-based methodologies used by engineers, and will provide a basis for establishing equation-of-state relationships for use in theoretical computations.

Finally, the conclusion of significant nonlinearity is good news in that the amplifying effects of sediments, on average, are apparently not as great as implied by weak-motion studies. However, it brings into question the use of empirical Green's functions (based on recordings of small earthquakes) to study or predict strong ground motion at sediment sites. □

Table 1 The 21 locations in the study region

Site name	Site geology*	Latitude	Longitude	Number of aftershocks	Ratio at 3 Hz†	PGA‡ (cm s^{-1})
CPC	alluvium	34.212	−118.605	53	1.77	538
JFP	alluvium	34.313	−118.498	32	7.98	616
LCN	alluvium	34.063	−118.418	57	1.99	251
HST	alluvium	34.090	−118.338	91	1.40	225
ALF	alluvium	34.070	−118.150	69	1.27	99
MPK	alluvium	34.288	−118.881	26	1.52	286
NWH	alluvium	34.390	−118.530	42	2.05	578
SFY	alluvium	34.236	−118.439	44	2.90	541
VSP	alluvium	34.249	−118.478	5	9.37	923
LVS	alluvium	34.005	−118.279	6	0.91	285
LSS	alluvium	34.046	−118.355	2	2.52	482
SYH	alluvium	34.326	−118.444	19	1.60	827
BHA	alluvium	34.009	−118.361	15	1.83	234
NRG	alluvium	34.209	−118.517	9	2.28	468
SMI	alluvium	34.264	−118.666	36	1.28	924
LF6	soft rock	34.132	−118.439	85	5.96	498
TOP	soft rock	34.084	−118.599	4	1.32	327
SSA	hard rock	34.231	−118.713	26	1.52	336
SCT	hard rock	34.106	−118.454	184	0.97	371
PCD	hard rock	34.334	−118.396	25	0.42	426
LWS	hard rock	34.089	−118.435	14	1.61	293

*As defined in the SCEC strong-motion data archive[17].
† The ratio of weak- to strong-motion site response estimate at 3 Hz.
‡ Peak ground acceleration observed during the Northridge main shock[17].

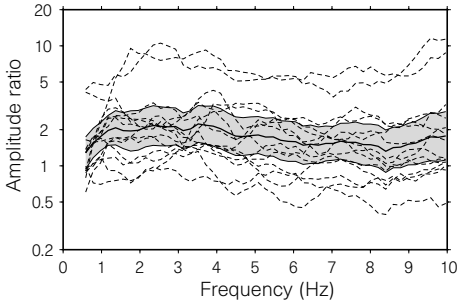

Figure 3 Ratios of the estimates of weak- to strong-motion site responses for each of the 15 sediment sites (dashed lines). The values at 3 Hz are listed in Table 1. The mean and 95% confidence region of all the sediment-site ratios are plotted with the solid lines and shaded region (based on a t-distribution with 14 degrees of freedom). The weak-motion amplification estimates are, on average, significantly higher, implying nonlinearity.

Received 22 April; accepted 23 September 1997.

1. Milne, J. *Seismology* 1st edn (Kegan Paul, Trench, Truber, London, 1898).
2. Aki, K. Local site effects on strong ground motion. *Proc. Earthq. Eng. Soil Dyn.* **II,** 103–155 (1988).
3. Bersenev, I. A. & Wen, K.-L. Nonlinear soil response—A reality? *Bull. Seismol. Soc. Am.* **86,** 1964–1978 (1997).
4. Aguirre, J. & Irikura, K. Preliminary analysis of non-linear site effects at Port Island array station during the 1995 Hyogoken–Nambu earthquake. *J. Nat. Dis. Sci.* **16,** 49–58 (1995).
5. Petersen, M. D. *et al.* Seismic ground-motion hazard mapping incorporating site effects for Los Angeles, Orange, and Ventura counties. *Bull. Seismol. Soc. Am.* **87,** 249–255 (1997).
6. Andrews, D. J. Objective determination of source parameters and similarity of earthquakes of different size. *Earthq. Source Mech. Geophys. Monogr. 37* **6,** 259–268 (1986).
7. Field, E. H. & Jacob, K. H. A comparison and test of various site response estimation techniques, including three that are not reference site dependent. *Bull. Seismol. Soc. Am.* **85,** 1127–1143 (1995).
8. Wald, D. J. *et al.* The slip history of the 1994 Northridge, California earthquake determined from strong-motion, teleseismic, GPS, and leveling data. *Bull. Seismol. Soc. Am.* **86,** S49–S70 (1996).
9. Archuleta, R. J. & Hartzell, S. H. Effects of fault finiteness on near-source ground motion. *Bull. Seismol. Soc. Am.* **71,** 939–957 (1981).
10. Heaton, T. H. Evidence for and implications of self-healing pulses of slip in earthquake rupture. *Phys. Earth Planet. Inter.* **64,** 1–20 (1990).
11. Hartzell, S. *et al.* Site resonse for urban Los Angeles using aftershocks of the Northridge earthquake. *Bull. Seismol. Soc. Am.* **86,** S168–S192 (1996).
12. Peng, J. Y. Spatial and temporal variation of coda Q in California. Thesis, Univ. South California, Los Angeles (1989).
13. Bonilla, L. F. *et al.* Site amplification in the San Fernando Valley, CA: Variability of site effect estimation using the S-wave, coda, and H/V methods. *Bull. Seismol. Soc. Am.* **87,** 710–730 (1997).
14. Cranswick, E. The information content of high-frequency seismograms and the near-surface geologic structure of "hard rock" recording sites. *Pure Appl. Geophys.* **128,** 333–363 (1988).
15. Steidl, J. *et al.* What is a reference site? *Bull. Seismol. Soc. Am.* **86,** 1733–1748 (1996).
16. Zeng, Y. & Anderson, J. G. A composite source model of the 1994 Northridge earth quake using genetic algorithms. *Bull. Seismol. Soc. Am.* **86,** S71–S83 (1996).
17. Strong-motion data archive of the Southern California Earthquake Center (web address: http://quake.crustal.ucsb.edu/scec/smdb/smdb.html).

18. Meremonte, M. *et al.* Urban seismology—Northridge after shocks recorded by multiscale arrays of portable digital seismographs. *Bull Seismol. Soc. Am.* **86,** 1350–1363 (1996).
19. Data Center of the Southern California Earthquake Center (web address: http://www.sceccdc.scec.org.).

Acknowledgements. We thank several members of the Los Alamos National Laboratory (LANL) and the Southern California Earthquake Centre (SCEC) for comments and discussions. The data used in this study were collected by the SCEC, the United States Geological Survey, the California Division of Mines and Geology, the University of Southern California, the Department of Energy, and the City of Los Angeles. This work was supported by LANL Institutional Support (LDRD-IP). E.H.F. received additional support from the SCEC.

Correspondence and requests for materials should be addressed to E.H.F. (e-mail: field@usc.edu).

Absence of contour linking in peripheral vision

Robert F. Hess & Steven C. Dakin

McGill Vision Research, Department of Ophthalmology, McGill University, Montreal, Quebec, H3A 1A1 Canada

Human foveal vision is subserved initially by groups of spatial, temporal and orientational 'filters', the outputs of which are combined to define perceptual objects. Although a great deal is known about the filtering properties of individual cortical cells, relatively little is known about the nature of this 'linking' process. One recent approach[1] has shown that the process can be thought of in terms of an association field whose strength is determined conjointly by the orientation and distance of the object. Here we describe a fundamental difference in this feature-linking process in central and peripheral parts of the visual field, which provides insight into the ways that foveal and peripheral visual perception differ[2,3]. In the fovea, performance can be explained only by intercellular linking operations whereas in the periphery intracellular filtering will suffice. This difference represents a substantial economy in cortical neuronal processing of peripheral visual information and may allow a recent theory of intercellular binding to be tested[4–7].

The way that distributed neuronal activity in the cortex is combined to define perceptual objects is an important question in neurobiology[7]. In human vision, one promising method of study involves the detection of paths of spatially narrowband elements embedded in a field of similar elements with random position and orientation[1]. The elements forming the path differ from those of the background in that they conform to first-order curves (Fig. 1). Human detection performance is nearly perfect for paths with orientation differences between neighbouring elements of up to 20–30 degrees (Fig. 1a). It has been claimed[1], but never substantiated, that such performance could not be supported solely by individual cortical filters, and hence requires an integrative or linking process between cells analysing different orientations. We find that this claim is indeed correct.

We used a path-detection model operating on multiple, independent oriented filter outputs (Fig. 2 and Methods). The image is initially orientation-filtered at a scale appropriate to the elements. After thresholding, a symbolic description of the resulting orientation features is computed (a two-dimensional adaptation of the MIRAGE algorithm[8]). The path is then indicated by the longest feature present across all orientations. In the example in Fig. 2 the path angle is zero and filters aligned with the straight path correctly encode the path perceived in Fig. 2.

The solid line in Fig. 3a represents the output of our filter model, compared with the performance of human foveal vision. Model performance is much worse than that of human subjects when path angle is increased and when the paths become more curved (Fig. 3a). We could find no method of improving the performance of the model without introducing interactions between cells tuned to different orientations, providing a quantitative demonstration that filtering alone (intracellular processing), at any one of a number of orientations, is insufficient to explain human performance. A direct test of this conclusion is to use paths composed of elements whose spatial phases are alternately switched by 180°, embedded in a background of elements with spatial phase set randomly to either 0° or 180°. Such a stimulus (Fig. 1b), which cannot be detected by a simple linear filtering operation (model results are shown as a solid

Figure 1 An example of the path stimuli used. **a**, All elements are localized in spatial frequency and are of cosine phase. The path, which is slightly curved, runs from bottom to top through the middle of the picture. **b**, A similar path, but now composed of similar elements alternating in spatial phase by 180°, curves from the bottom left to the top right, embedded in a background field of alternating-phase elements. In the fovea both types of path are easily detected, but in the periphery, the path shown in **b** is invisible.

Figure 2 The simple-filter model. **a**, An example image. **b**, The operation of four filters from the full bank of 12 is shown. **c**, These filter outputs are 'thresholded' (all grey levels falling within ±1 s.d. of the mean are replaced with the mean value), producing a new image containing both positive and negative polarity 'blobs' (here blobs have been contrast-enhanced to demarcate them further). **d**, Descriptions of the 'blobs' in each of these images, by which it is possible to identify the longest blob across all filter outputs, identified as the 'path'.